Received: 21 September 2022 | Revised: 24 November 2022 | Accepted: 6 December 2022

DOI: 10.1002/pc.27210

RESEARCH ARTICLE

Polymer COMPOSITES WILEY

Visualizing pseudo-ductility in carbon/glass fiber hybrid composites manufactured using infusible thermoplastic Elium® resin

Tayyab Khan | **Muhammad A. Ali** | **Muhammad S. Irfan** | **Wesley J. Cantwell** | **Umer Rehan**

Department of Aerospace Engineering, Khalifa University of Science and Technology, Abu Dhabi, UAE

Correspondence
Umer Rehan, Department of Aerospace Engineering, Khalifa University of Science and Technology, P.O. Box 127788, Abu Dhabi, UAE.
Email: rehan.umer@ku.ac.ae

Funding information
Khalifa University of Science, Technology and Research, Grant/Award Number: CIRA-2020-007

Abstract

In this study, two different type of glass and carbon fiber hybrid laminates were manufactured using a low-viscosity thermoplastic resin that is, Elium®. A detailed microstructure visualization study was conducted using X-ray computed tomography (XCT) analysis. The viscoelastic properties were examined through dynamic mechanical analysis. The mechanical performance was investigated through flexural and tensile tests along with a fractographic study using optical and scanning electron microscopy. The XCT analysis revealed a weak interface between the Elium® resin and the glass fabric, with glass fiber specimens exhibiting a void content of 1.24%, in contrast to the carbon fiber specimens which showed void content of only 0.28%. Therefore, adding glass fabric layers in the hybrid laminates increased the void content, which had a negative impact on the overall mechanical performance. The average flexural strength of the hybrid specimen having $G_2C_4G_2$ stacking sequence was observed to be 254% higher than pure GFRPC specimens. Similarly, the tensile strength and Young's modulus of the same hybrid specimen showed 155% and 380% increases, respectively, compared to the GFRPC specimens. This increase was primarily due to higher stiffness of the carbon fibers and their better fiber – matrix interface. Whereas the tensile strain of the hybrid specimen having $G_3C_2G_3$ stacking sequence was 37% higher than that of the CFRPC specimens. The SEM images highlighted fiber fracture and brittle failure modes in the carbon fiber specimens, in contrast to fiber pullout, interfacial failure, poor fiber-matrix bonding and ductile failure modes in the glass fiber specimens.

KEYWORDS

hybrid laminates, pseudo-ductility, thermomechanical behavior, thermoplastics, XCT

1 | INTRODUCTION

Fiber reinforced polymer composites (FRPC) have become significantly popular in multiple structural applications over past few decades due to their unique properties such as, high strength and stiffness, fatigue durability, low density and high corrosion, and chemical resistance.[1–3] In fact, FRPCs are better alternatives to the conventional structural materials like metals, especially in the automotive, aerospace, construction and marine industries, and this trend is to continue as a consequence of their superior mechanical properties.[4–6] Among the different types of FRPCs, carbon fiber reinforced polymer composites (CFRPCs) have emerged as state-of-the-art material in modern aviation, automotive and wind energy applications due to their lightweight, dimensional stability, low thermal expansion and unprecedented mechanical properties such as high specific strength and stiffness and superior impact energy absorption.[7,8] Nevertheless, the most considerable disadvantage associated with CFRPCs is their sudden catastrophic failure with little or no prior warning due to limited failure strain, brittle nature and lack of plastic deformation.[9] Consequently, composite structures are often oversized to ensure safety and as a result, their excellent strength to weight ratio is not fully exploited.[10]

Hybridization is one the most effective techniques to avoid any catastrophic failure and ensure metal-like plastic deformation in high-performance CFRPCs. Hybrid FRPCs generally refer to a class of composite materials with two different types of fibers reinforced within a single polymer matrix.[11–17] Hybridization of high-strain fibers, for example, glass fiber (GF) and high-strength fibers such as carbon fiber (CF) can ensure high strength as well as high failure.[18,19] Carbon fibers are well-known for their high strength, which is even higher than that of some metals, but suffer from brittleness and exhibit low tensile failure strain ranging from 0.4% to 2.4%.[20,21] On the other hand, GFs are characterized by high ductility, having failure strain as high as 5.2%.[20] Therefore, carbon/glass hybridization can introduce plastic deformation by increasing the percent elongation (pseudo ductility) in the CFRPC composites and suppress their catastrophic failure mode.[22,23] Over the years, pseudo ductile hybrid composites with two different types of fibers have been achieved in three distinct ways: (1) interlayer, (2) intralayer and (3) fiber-by-fiber or intrayarn configurations.[24] A number of studies have been reported over the years to achieve pseudo ductility in FRPCs.[16,25] Promising results of hybridization have also been reported for other materials.[26–30] Another promising approach for hybridizing is the use of two different type of weave structures which can significantly reduce the resin-rich areas because of different weave architecture (i.e., nesting effect). As a result, hybrid composite laminates having dissimilar weave architectures have a higher reinforcement packing density, higher fiber weight fraction (FWF), and ultimately, superior mechanical performance.[17]

Significant developments have been made in the past decade on pseudo-ductile carbon/glass hybrid composites, and it has been well-established through multiple numerical and experimental studies that optimal pseudo-ductile response can be achieved with interlayer configurations where high strain GF layers surround a thin ply of the low strain CF layers in a hybrid laminate.[31,32] For example, Czél et al.[33] prepared different thin-ply carbon/glass hybrid composite specimens and reported stress–strain responses in hybrid specimens that resembled those observed in ductile metals. The hybrid specimens exhibited pseudo ductile strain as high as 2.64% compared to that exhibited by pure glass fiber reinforced polymer composites (GFRPCs). At the same time, the hybrid specimens exhibited high initial modulus of up to 124 GPa, similar to that of high strength CFRPC specimens, primarily due to hybridization with the S-glass fabrics. Similarly, Jalalvand et al.[31] reported 1% pseudo strain in carbon/glass hybrid composites exhibiting nonmetal-like stress–strain curves with a progress tensile failure mode. A number of other studies have reported similar pseudo-ductile behavior in carbon/glass hybrid composite laminates by stacking high strain glass fabrics as outer layers to the high strength inner carbon layers.[34]

In recent years, considerate effort has been made to move toward efficient design[35] and sustainable composites manufacturing, where scientists and industrial partners across the globe are looking toward thermoplastics as an alternative to non-recyclable thermosetting resins. This transition toward thermoplastics is driven by multiple advantages, such as recyclability, post-formability, high chemical resistance, superior energy absorption capability and unlimited shelf-life.[36,37] Considering all these advantages, a number of thermoplastic reactive systems compatible with resin transfer molding (RTM) process have been developed in recent years. These reactive thermoplastic systems include polyamide (PA) 6, PA 12, poly(butylene terephthalate) (PBT), and more recently, polymethymethacrylate (PMMA).[38] In terms of low-viscosity thermoplastic resins, Arkema Industries is pioneer in developing a range of novel infusible thermoplastic resins under the trade name Elium®, having low viscosities ranging from 100–200 mPa.s, that is, comparable to those of thermosetting liquid resins.[39]

Ever since its introduction, significant research has been conducted on Elium® based composites, reporting

major breakthroughs in terms of mechanical performance,[37,40] thermomechanical properties,[41] recyclability,[42] thermoformability[42] and weldability.[43] In fact, a preliminary study on the hybridization of Elium®-based composites comprising carbon and ultra-high molecule weight polyethylene fiber (UHMWPE) has also been reported in the literature.[44] The authors reported mechanical performance of the hybrid composites in terms of tensile, compressive and shear properties. A comprehensive review on Elium®-based composites is also available in the literature.[45] While comprehensive studies have been conducted on the pseudo-ductile response of multiple thermoplastic composites, such as polypropylene (PP), polycarbonate, and polyurethane, and so forth, the true potential of Elium®-based carbon/glass hybrid composites, in terms of pseudo ductility and the effect of hybridization on the microstructure, has not been explored yet.

In this article, two different types of hybrid composite specimens were manufactured along with pure CFRPC and GFRPC specimens to investigate the microstructural changes and mechanical performance in infusible thermoplastic composites based on Elium® resin. A detailed XCT study was conducted to visualize the microstructure of the composite specimens in terms of fiber volume fraction and defects, such as voids and porosity. The thermal stability of specimens was investigated by the TGA analysis and the thermomechanical properties were examined by conducting the DMA tests. The mechanical performance was investigated in detail through flexural and tensile tests, and the fractographic study comprised of optical and scanning electron microscopy (SEM). The primary objective of the study is to investigate, for the first time, pseudo ductile response of Elium®-based hybrid composites. Another aim of this study is to visualize the fiber – matrix interaction at a microscopic level through comprehensive XCT and SEM analysis. The results of this research are expected to fill potential research gaps in the literature in terms of microstructural analyses, thermomechanical properties, mechanical performance, thermal stability and fractographic analysis of infusible thermoplastic resin based hybrid composites.

2 | MATERIALS AND METHODS

2.1 | Materials

Four different types of composites, comprising of carbon and glass fibers were manufactured. 3 K-CFs having a (2 × 2) twill weave architecture and (plain weave) E-glass fibers, provided by Gurit®, United Kingdom, were used. The fabrics were reinforced with an infusible thermoplastic resin that is, Elium® 188 O, supplied by Arkema, China. Luperox® ATC50 benzoyl per oxide (BPO) initiator provided by Sigma-Aldrich Corporation, was used to initiate the polymerization of the infusible resin.

2.2 | Methods

2.2.1 | Manufacturing of laminates

The composite laminates were manufactured through the VARTM or resin infusion process. Four different types of composite specimen, comprising of 8 fabric layers, were manufactured that is, CFRPC (C_8), GFRPC (G_8), $G_2C_4G_2$ hybrid laminates referred to as H1 and $G_3C_2G_3$ hybrid laminates referred to as H2, as shown in Figure 1A. A glass mold was first prepared by applying the release wax, followed by the placement of the fabric layers, peel-ply and flow-mesh. After that, resin supply line and outlet connections were connected. Finally, the setup was sealed using a vacuum bag and tacky tape. For all the infusion setups, 1.5% BPO initiator was mixed with the thermoplastic resin and the mixture was carefully stirred for 5 min as degassing is not advised for Elium® 188 O. VARTM manufacturing was performed at the ambient temperature, and the laminates were cured at the same temperature for 24 h. After that, the composite laminates were post-cured at 60°C for 24 h. The optical micrographs of all the specimens after manufacturing are shown in Figure 1B.

2.2.2 | XCT analysis

The quality of the manufactured specimens was investigated through a comprehensive Xray computed tomography (XCT) analysis by using the GE Phoenix Nanotom® XCT machine.[46–48] Rectangular samples, with an area of 10 × 50 mm^2, were cut from the composite laminates and scanned for comparison in terms of fiber volume fraction, porosity, void content and the amount of defects. A total of 460 radiographic images were captured during the 360° rotation of the sample at a scan resolution of 10 μm. The raw XCT images were then reconstructed into three-dimensional (3D) gray scale volumes. To visualize the individual components of the laminate that is, fibers, resin and cracks/voids, the greyscale raw volume was segmented using the GeoDict® analysis software package. Global thresholding values were used for the segmentation of the gray scale volume.[49] The segmented models were used to evaluate the volume contents of each of the constituents that is, fibers, resin and voids.

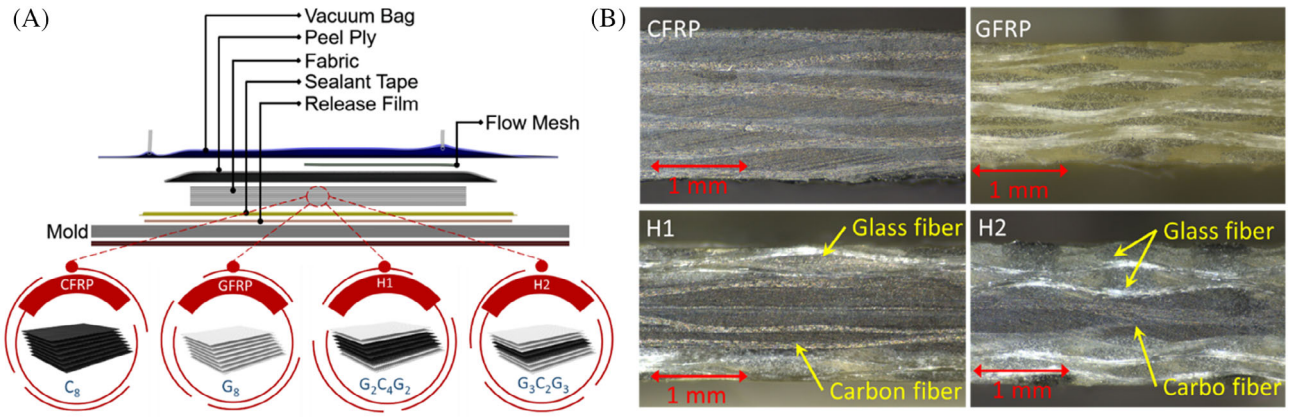

FIGURE 1 (A) General layout of the VARTM manufacturing process along with fabric stacking sequence and (B) optical cross-sectional micrographs of the specimens

2.2.3 | Thermogravimetric analysis

Thermogravimetric analysis (TGA) of all the samples was conducted by using the TA SDT Q600 instrument. TGA analysis is widely used to investigate the thermal stability of materials and to evaluate the FWF of composite specimens. The TGA scans were conducted as constant flow rate of 20 ml/min using nitrogen. The heating rate was kept constant as 10°C/min and the scans were performed from 28 to 999°C. Al_2O_3 pans were used for all the specimens due to their higher thermal stability and the sample mass was around 10 mg.

2.2.4 | Dynamic mechanical analysis

Dynamic mechanical analysis (DMA) tests were conducted using the NETZSCH DMA 242 E Artemis testing equipment. The tests were conducted in three-point bending mode using the temperature ramp program at a constant frequency of 1 Hz. The temperature was varied from 30 to 150°C at a constant heating rate of 3°C/min, applying a dynamic amplitude of 15 μm. The span of the samples during all the tests was kept constant as 40 mm. At least three samples were tested for each configuration, and all the tests were conducted according to the ASTM D5023-15 test standard. The glass transition temperature (T_g) for all the specimens was calculated from the Tan δ peaks. Tan δ is a derived property and is a ratio of storage modulus to loss modulus, as expressed by Equation 1.

$$\text{Tan}\,\delta = \frac{E'}{E''} \tag{1}$$

2.2.5 | Flexural tests

The flexural properties of all the composite specimens were evaluated by subjecting them to three-point bending tests. The tests were conducted using an Instron-5969 UTM machine with a load-cell capacity of 5 kN. The span-thickness ratio was kept constant as 32:1. The test were conducted a constant speed of 1 mm/min and all the tests were performed in accordance with the ASTM D790-17 test standard. The standard deviation in the results was calculated by using the 95% confidence interval (CI) formula, that is, $(\pm 1.96 \times SD/\sqrt{n})$, n is the number of samples and SD is the standard deviation.[50] The experimental setup for the three-point bending tests is shown in Figure 2B, whereas the dimensions of the test specimens are provided in Figure 2C.

2.2.6 | Tensile tests

Tensile tests were also conducted on an Instron-5969 UTM having a load-cell of 50 kN and the experiments were conducted in accordance with the ASTM D3039/D3039M-17 standard. To avoid the clamping damage, 40 × 25 mm^2 GFRPC end tabs were adhesively bonded on both sides of the test specimen. The tests were performed at a constant speed of 2 mm/min and at least five specimens were tested for each configuration. The tensile strain was calculated through digital image correlation (DIC) mechanism as well through an extensometer by creating random speckles throughout the gauge length of the specimens using white spray paint and creating extensometer markers on the specimens.

Digital image correlation

The DIC method is one of the widely used non-contact, full-field actual strain measuring techniques, independent of specimen dimensions.[51] In terms of the basic working principle, the DIC technique tracks the

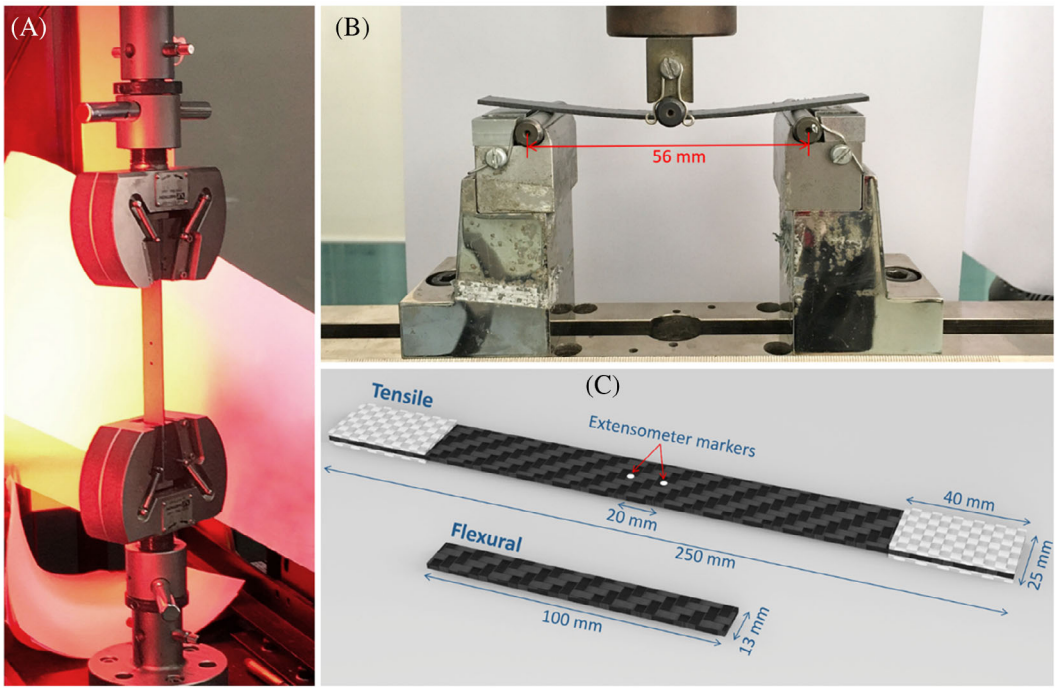

FIGURE 2 (A) Experimental setup for tensile tests, (B) three-point bending test setup and (C) dimensions of tensile flexural test specimens

movement of randomly distributed points and compares the location of these points before and after the deformed state.[51,52] Therefore, random texture (speckles) are created on the test specimens by spraying them with white paint. As the specimens are loaded, these random points also deform and carry the deformation history. The surface of the specimens is well-illuminated with light (as shown in Figure 2A). A camera attached to the UTM is connected to a computer which stores the acquired images throughout the test. The stored images are then post-processed by the Intron® 2D DIC Replay software which readily provides the true strain. The DIC method is extensively preferred especially in solid mechanics over different interferometric methods.[53]

2.2.7 | Scanning electron microscopy

The fractographic study was conducted by using the scanning electron microscopy (SEM) using the FEI Quanta 250 FEG-SEM. The SEM analysis was performed to further investigate the microstructure of the composite laminates and correlate the results with the XCT analysis. The fractured specimens subjected to the 3-poin bending tests were thoroughly examined to investigate the degree of interfacial adhesion, compare the failure modes and observe the fiber-matrix interface at a microscopic level.

3 | RESULTS AND DISCUSSION

3.1 | XCT analysis

The microstructure of all the composite specimens was investigated by examining the XCT images. Different slices from the raw volumes were initially considered to understand the effect of hybridization on the microstructure, fiber-matrix bonding and mesoscopic defects. Additionally, 3D models of the composite laminates were created from the raw XCT images using the GeoDict® software and then the region of interest (ROI) was created in the central portion of the voxel geometry. These 3D models were used to conduct a statistical analysis in terms of fiber volume fraction, resin volume fraction and crack/porosity content in all type of composites. The 3D models generated from the raw images for CFRPC and GFRPC samples are presented in Figure 3A,C, respectively, where the gray regions correspond to the fabrics, yellow regions represent the Elium® resin, and cracks/porosity are highlighted in red color. In addition, the porosity content and the void fraction in both CFRPC and GFRPC samples are separately presented in Figure 3B,D, respectively. Top-view from random slices of the raw XCT images for the GFRPC specimens are shown in Figure 3E,F. The blue regions in the raw XCT images represent the fabrics, the yellow regions represent the Elium® resin, and the voids/porosity are highlighted

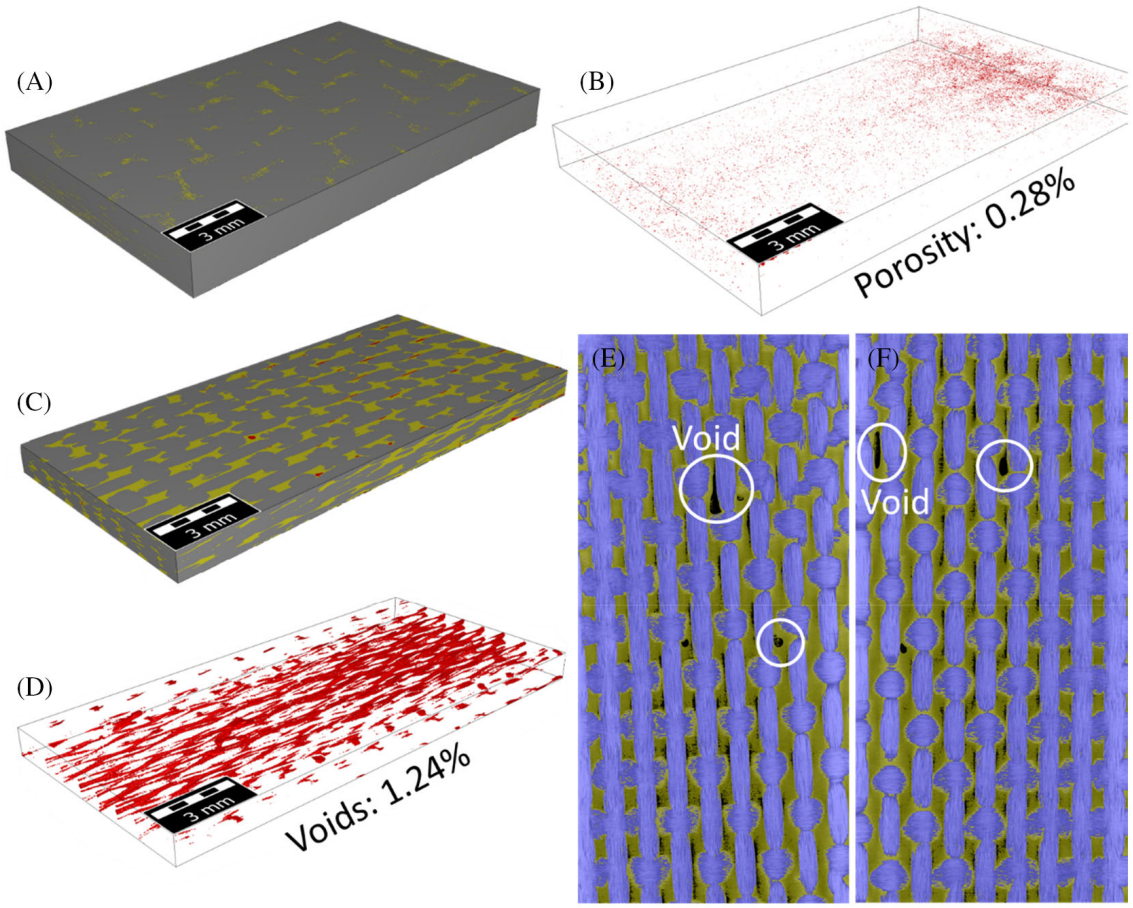

FIGURE 3 Xray computed tomography results (A, B) 3D models for carbon fiber reinforced polymer composites (CFRPC) specimens, (C, D) 3D models for GFRPC specimens and (E, F) top-view of raw images for GFRPC specimens

TABLE 1 Material properties of composite specimens found through XCT analysis

Sample	Solid fiber volume fraction (SVF) (%)		Resin volume fraction (%)	Void content (%)
	Carbon	Glass		
CFRPC	76.88 ± 1.4	–	22.84 ± 1.2	0.28 ± 0.01
H1	33.6 ± 0.8	32.83 ± 0.7	32.67 ± 1.2	0.90 ± 0.2
H2	22.46 ± 0.3	38.9 ± 0.5	37.43 ± 0.6	1.20 ± 0.2
GFRPC	–	69.6 ± 2.1	29.16 ± 1.8	1.24 ± 0.3

in black color. The statistical results of the microstructural investigation for all the composite specimens are provided in Table 1.

The 3D models revealed that the overall porosity content in the CFRPC specimens was only 0.28% and there were no micro/macro level voids in the ROI. In contrast, the GFRPC specimens exhibited microstructural defects in the form of voids, mainly concentrated along the edges of glass fiber tows (Figure 3E,F). The overall void content in the GFRPC specimens was found to be 1.24%. These voids in the GFRPC specimens clearly demonstrate a weak glass fiber-Elium® interface, which is also observed through the SEM analysis, as discussed in Section 3.6. Another important factor that plays a key role in determining the fiber-matrix interface properties is the fiber sizing. A preliminary study on Elium® resin has demonstrated that the epoxy-sized fibers that are compatible with the conventional thermosetting resins are soluble in the reactive MMA monomer.[54] Therefore, the solubility of the glass fiber sizing is another possibility for weaker fiber-matrix interface. It is well-known that the sizing formulations for glass fibers are far more complex than those for carbon fibers as they require a silane component to build the bond between glass fibers and polymer.

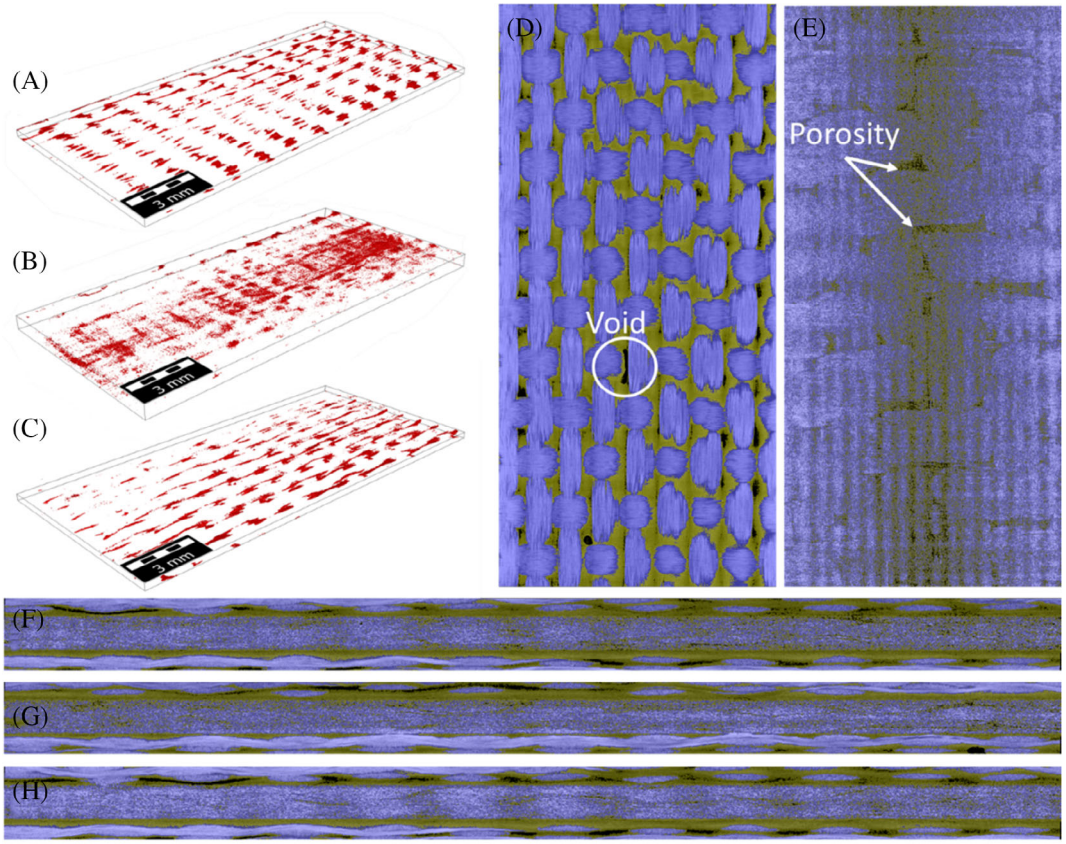

FIGURE 4 Xray computed tomography results for H1 specimens (A–C) 3D model showing void content and porosity, (D, E) top view of raw images and (F–H) cross-sectional raw images

This is not an issue with carbon fibers as low-viscosity resins are inherently sticky and wet the organic carbon fibers quite well.[55] However, it should be noted that the proprietary nature of fiber sizings, their formulation and constituents are highly protected. Based on secrecy in this field, it is almost impossible to determine the precise chemical properties and role of fiber sizing.[54] Another possible reason for high void content in the GFRPC specimens is the high weave density, which in turn reduces the permeability of the preform and leads to weak interfacial bonding and improper impregnation.[17] Such a high void content had a major influence on the mechanical performance of the GFRPC as well as the hybrid composites.

As a result of hybridization, the void content in both types of hybrid specimens was substantially increased compared to the CFRPC specimens. The 3D models and the raw XCT images for H1 specimen are shown in Figure 4. The 3D models showing the microstructural defects were also segmented based on the type of the fabric reinforcement by counting the number of slices. The voids in the top and bottom glass fabric layers are shown in Figure 4A,C, respectively. Whereas the porosity in the central carbon fabric regions of the H1 specimens is shown in Figure 4B. A further investigation of the raw XCT images in Figure 4 illustrated that the voids were primarily constrained in the glass fabric regions whereas the middle carbon layers only exhibited micro porosity. Again, the cross-sectional XCT images in Figure 4 show that the voids in the top and bottom sections of the glass fabric regions were mainly confined along the edges of tows, showing poor bonding of Elium® resin with glass fabrics. The overall void/porosity content in the H1 specimens was recorded as 0.90%.

A similar trend was observed in the H2 hybrid specimens, where the voids were mostly confined in the glass fabric regions, whereas the central carbon regions only exhibited microporosity. The cross-sectional XCT images in Figure 5 show that increasing the number of glass fabrics again increased the void content compared to the H1 specimens. The overall void/porosity content in the H2 specimens was found to be 1.20%, similar to that recorded for the pure GFRPC specimens (1.24%). The carbon fabric regions again exhibited microporosity with no visible voids. It is also evident that the porosity in the carbon fabric regions of both H1 and H2 specimens substantially increased compared to that recorded in pure CFRPC specimens. This is mainly due to the greater resistance to

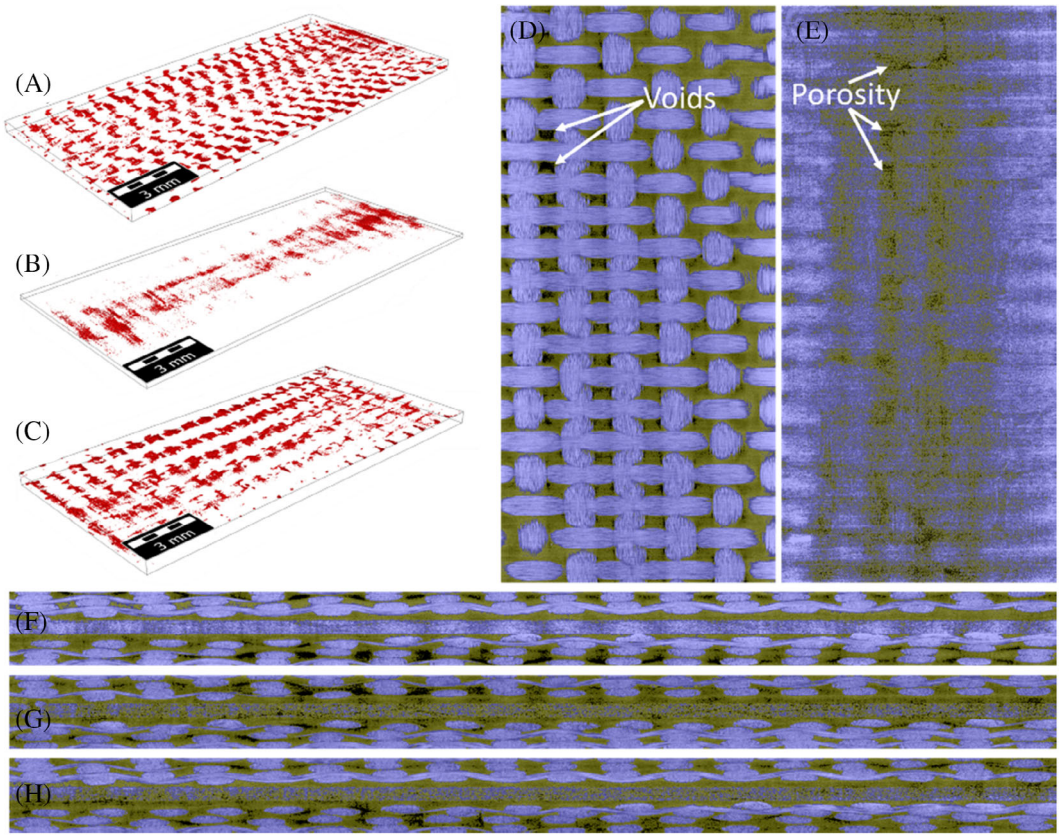

FIGURE 5 Xray computed tomography results for H2 specimens (A–C) 3D model showing void content and porosity, (D, E) top view of raw images and (F–H) cross-sectional raw images

the through thickness flow in both directions due to the presence of glass fabrics with high weave density.

It is important to note that the void content in H1 specimens was significantly decreased unlike in the H2 specimens ($G_3C_2G_3$). This is primarily due to an increase in the glass fiber content in the H2 specimens. A decrease in carbon content in the H2 specimens from 33.6% to 22.46% compared to the H1 specimens does not have a major effect on the overall void content, as most of the voids are concentrated in the glass fiber regions. Therefore, an increase in the glass fiber content of H2 specimens from 32.83% to 38.9% compared to the H1 specimens increases the overall void content from 0.90% to 1.20%. Furthermore, increased number of glass fibers on both sides of carbon fibers in the H2 specimens provide more through thickness resistance, hence, leading to increased porosity in carbon fiber regions of H2 specimens compared to H1 specimens. Similarly, both carbon fabric regions in both hybrid configurations show greater porosity content than in CFRP specimens. The statistical results from the XCT analysis are provided in Table 1. It is important to note that the fiber volume fraction is presented in terms of the solid volume fraction (SVF). The SVF is defined as the ratio of the solid tows to the total volume of the specimen or ROI.[56,57] In contrast to the fiber volume fraction, the SVF provides a better estimation of the solid fiber tows and includes the impregnated resin content within the individual tows.

3.2 | Thermogravimetric analysis

Thermogravimetric analysis was performed to evaluate the thermal stability of all the specimens and to calculate the FWFs. The TGA curves, in terms of percentage weight loss against the applied temperature, for all the specimens are shown in Figure 6A. Whereas the derivative thermogravimetric (DTG) curves showing the rate of change of mass against temperature are shown in Figure 6B. It can be observed that the curves for CFRPC, H1 and H2 specimens show three distinct drops. The initial drop (labeled as 1) in weight percentage of all the specimens from 30 to 280°C is due to the dehydration phenomenon and is around 5% of the total weight drop.[2,17] Figure 6 reveals that a further increase in temperature resulted in a steep drop in weight from 280 to 400°C (point labeled as 2). This sudden drop represents the degradation of Elium® due to breakage of the polymer chains.[2] It is important to note

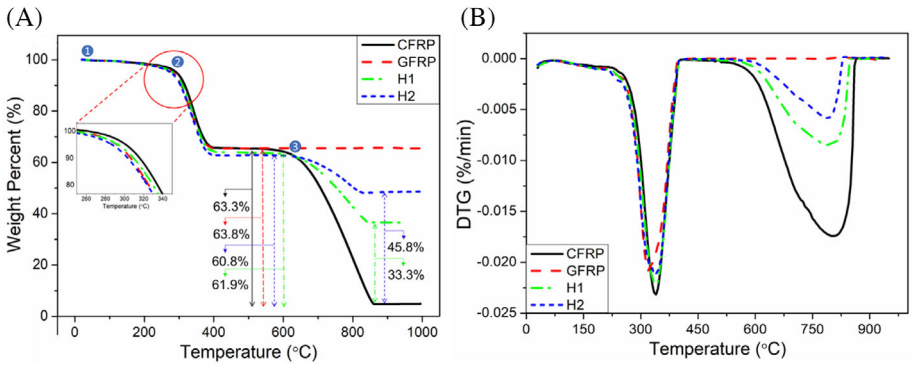

FIGURE 6 Thermogravimetric analysis (TGA) results (A) TGA curves showing weight loss and fiber weight fractions and (B) derivative thermogravimetric (DTG) curves showing rate of change of mass against temperature

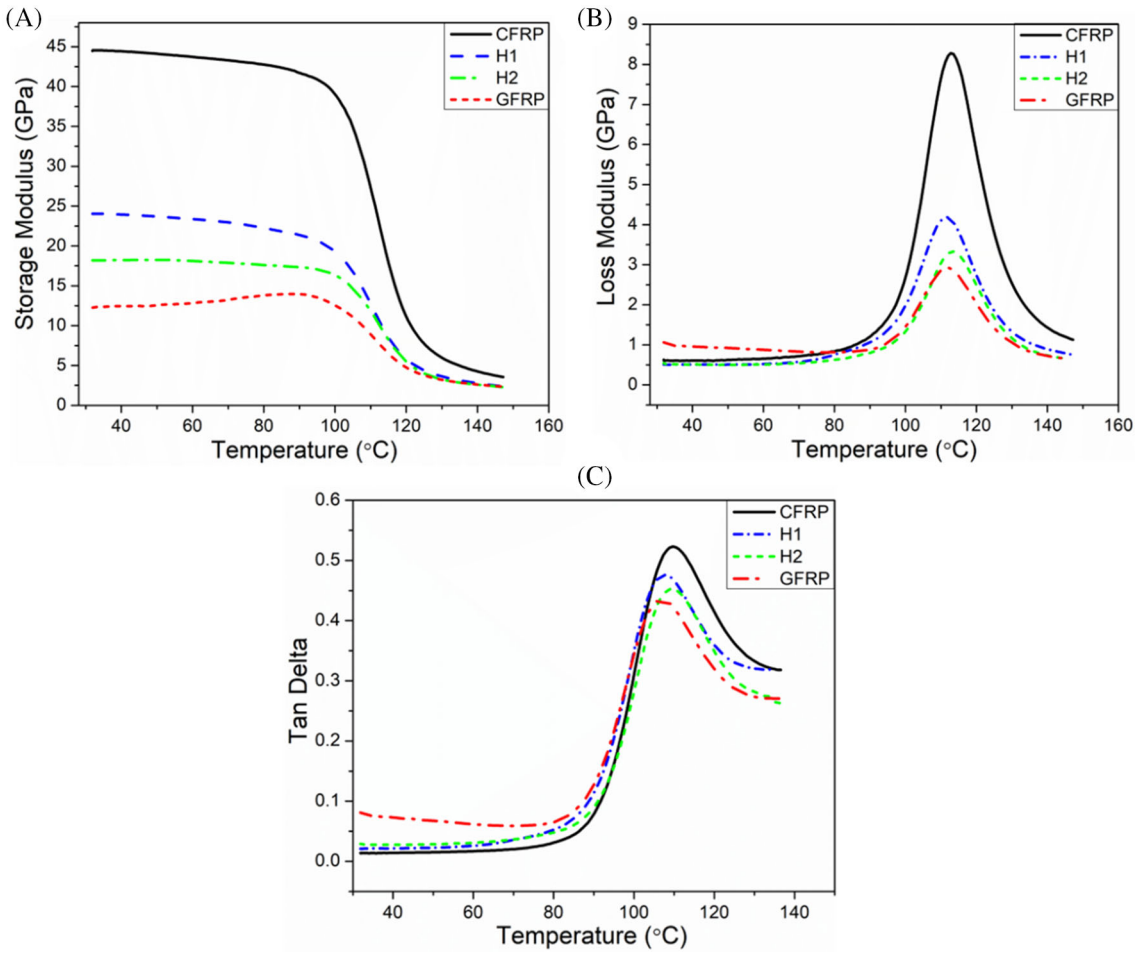

FIGURE 7 Thermomechanical properties (A) storage modulus, (B) loss modulus and (C) tan delta

that the Elium® resin starts to degrade at 280°C, critical temperature for the degradation of the thermoplastic matrix. The plateau between 400 and 600°C for all the specimens represents the fiber weight fraction after complete degradation of the Elium® resin. As the temperature is further increased, a final drop in weight of the specimens is observed from 600 to 850°C (point labeled as 3), representing the degradation of the carbon fibers. The weight loss curve for CFRPC specimens drops to zero percent at 850°C, whereas those of H1 and H2 drop to 33.3% and 45.8%, respectively, representing the weight percent of glass fibers in the hybrid specimens. It is obvious from Figure 6 that the GFRPC curves exhibits no drop beyond 400°C until 1000°C. This is due the high thermal stability of the silica (SiO_2) based glass fibers which do not degrade over the applied temperature range.[17] Therefore, the residue after 400°C represents the FWFs of the glass fibers in GFRPC specimens.

TABLE 2 Viscoelastic properties of composite specimens

Viscoelastic properties	Specimen			
	CFRPC	H1	H2	GFRPC
Storage modulus (GPa)	44.5 ± 0.41	24 ± 0.78	18.3 ± 0.12	14 ± 0.70
Loss modulus (GPa)	8.3 ± 0.15	4.2 ± 0.14	3.3 ± 0.08	3 ± 0.06
Tan delta (GPa)	0.53 ± 0.02	0.47 ± 0.01	0.45 ± 0.01	0.43 ± 0.01
Glass transition temperature (°C)	119 ± 0.50	115 ± 0.50	116 ± 0.25	114 ± 1.25

3.3 | Dynamic mechanical analysis

A series of DMA tests were performed on the composite specimens to examine their viscoelastic properties. The storage moduli curves for all the configurations are presented in Figure 7A, whereas the loss moduli and the tan delta curves are presented in Figure 7B,C, respectively. The maximum values of the storage moduli, loss moduli, and the T_g corresponding to the tan delta peaks were calculated from these curves. The average values of all these viscoelastic parameters are given in Table 2. The highest values of the storage moduli were recorded at room temperature in the glassy state where the components were closely packed and had low mobility, experiencing stronger intermolecular forces, hence, higher stiffness values. The storage modulus gradually decreased as the applied temperature was increased before approaching the T_g. As the T_g value was achieved, a sharp drop in the storage moduli for all the samples was recorded due to transition from glassy to rubbery state.

As expected, the highest storage modulus among all the thermoplastic composites was recorded on the CFRPC specimens, this being 44.5 GPa, reflecting the high stiffness of CFRPC specimens. As the outer layers of the CFRPC specimens were replaced by glass fabrics in the H1 specimens, the stiffness was compromised by around 46% and reduced to 24 GPa. As the glass fiber content was further increased, the average value of the storage modulus dropped to 18.3 GPa in H2 specimens. The lowest value of storage modulus was recorded for GFRPC samples as 14 GPa. It is important to note that hybridization of GFRPC specimens lead a substantial improvement in stiffness, where the H1 specimens exhibited around 72% increase in the storage modulus compared to GFRPC specimens. This improvement is attributed to the higher stiffness of the carbon fibers as well as to the stronger carbon fiber – matrix interface, as discussed in detail in Section 3.6.

A similar trend was observed in the loss moduli of the thermoplastic composites. The maximum value was found to be 8.3 GPa for the CFRPC specimens, whereas the lowest value was found to be 3 GPa for GFRPC specimens. Additionally, the tan delta peaks also showed a similar trend. Tan delta is the ratio of the loss modulus to the storage modulus and it is the measure of the energy absorption and dissipation of a material. The highest value of tan delta was recorded as 0.53 for CFRPC specimens, and it dropped as a result of hybridization with glass fibers, approaching a minimum value of 0.43 for pure GFRPC specimens. As a common practice, the T_g of the specimens is accurately calculated from the tan delta peaks. The curves in Figure 7C and the average results in Table 2 show that the highest T_g was observed as 119°C for CFRPC specimens. Whereas a slight drop in the T_g was recorded for both hybrid specimens, exhibiting a similar temperature for glass transition. However, the lowest value was recorded for GFRPC specimens as 114°C, showing a 5°C decrease compared to the CFRPC specimens. It has been well-established in the literature that the higher T_g of the CFRPC specimens compared to the GFRPC specimens is primarily due to higher stiffness of CFs, which further confines the movement of the polymer chains and delay the transition phase.[58] The DMA results for the thermoplastic composites are in good agreement with those reported in the literature for epoxy composites with a similar fabric architecture.[17] Furthermore, the values of the storage moduli are also comparable with the flexural and the tensile moduli of the composite specimens, as discussed in detail in the subsequent sections.

3.4 | Flexural tests

The load – displacement curves for 3-point bending tests on the thermoplastic composite specimens are given in Figure 8A, whereas a comparison of the flexural response for CFRPC and GFRPC thermoplastic composites with conventional epoxy counterparts is given in Figure 8B,C, respectively. The maximum flexural strength (σ) of the composite specimens was calculated based on the relative ASTM standard using Equation 2.[59]

$$\sigma = \frac{3PL}{2bd^2} \quad (2)$$

Where, P is the peak load, L is the support span, b is the width and d is the thickness of the specimen. The average

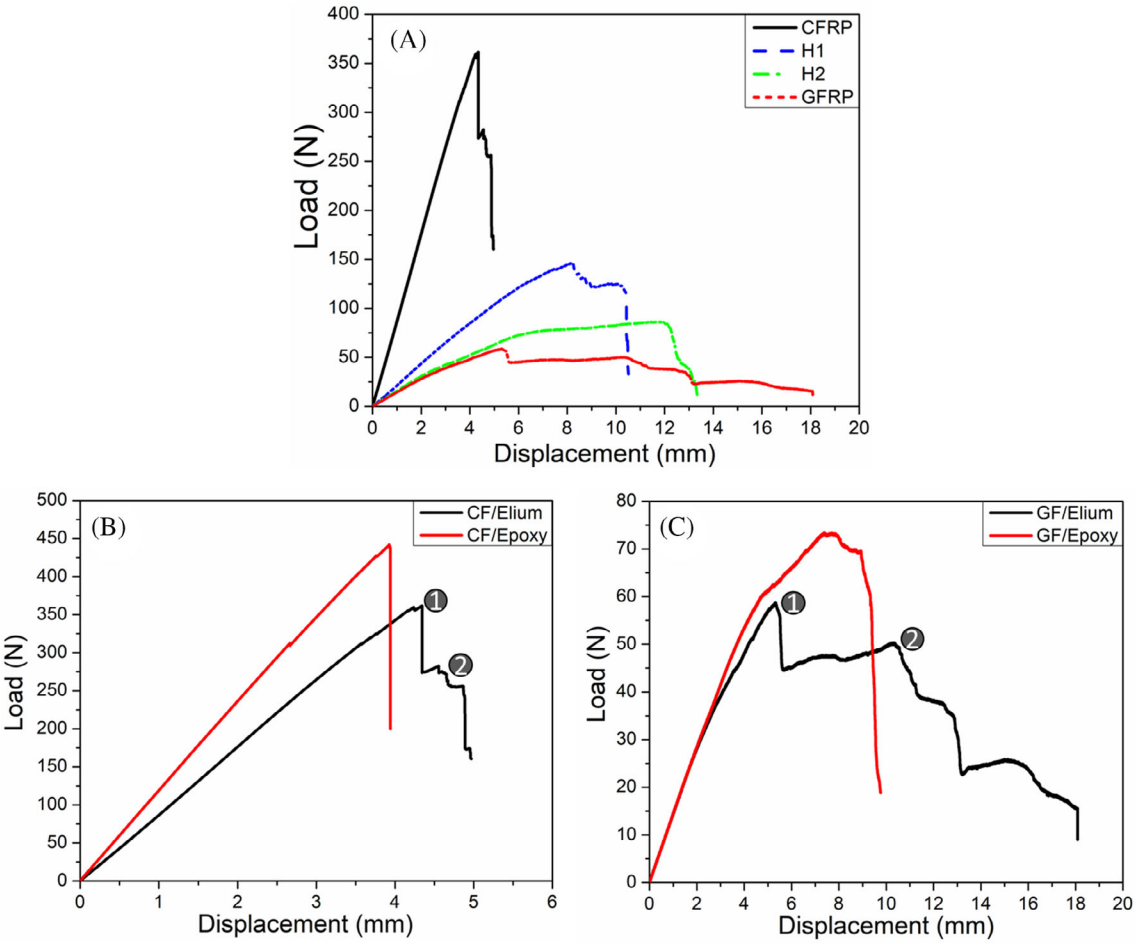

FIGURE 8 Flexural test results (A) load – displacement curves for all the specimens, (B) comparison between carbon/Elium® and carbon/epoxy composites and (C) comparison between glass/Elium® and glass/epoxy composites

TABLE 3 Flexural properties of composite specimens

Specimen	CFRPC	H1	H2	GFRPC
Peak load (N)	360 ± 1.9	138 ± 6.3	84 ± 4.6	61 ± 0.3
Max. flexural stress (MPa)	658 ± 3.8	449 ± 12.3	281 ± 4.2	127 ± 3.4
Flexural modulus (GPa)	50 ± 1.5	26 ± 2.1	14 ± 0.4	12 ± 0.5
Flexural strain (%)	1.37 ± 0.1	2.92 ± 0.3	3.97 ± 0.4	5.16 ± 0.3

values of the peak loads, flexural strengths and flexural moduli for all specimens, along with standard deviations, are given in Table 3.

The flexural tests revealed that the lowest flexural performance, in terms of flexural strength and flexural modulus, was exhibited by GFRPC specimens. Nevertheless, the highest displacement prior to failure was exhibited by GFRPC specimens, confirming their ductile nature. The average flexural strength of the H2 specimens was observed to increase from 127 to 281 MPa (over 121% increase) by introducing only two carbon fiber layers. Additionally, the H2 specimens exhibited a fairly ductile response, similar to GFRPC specimens despite a notable increase in strength. The flexural performance of the H1 specimens was further improved by increasing the number of carbon layers. The H1 specimens exhibited an average flexural strength of 449 MPa and average flexural modulus of 25.8 GPa, around 254% increase and 110% increase compared to the GFRPC specimens, respectively. As expected, CFRPC composite specimens exhibited superior flexural performance compared to all the specimens. The average flexural strength of CFRPC specimens was recorded to be 658 MPa, whereas the average flexural modulus was recorded as 50 GPa. However, the CFRPC specimens exhibited a catastrophic brittle failure mode compared to all other specimens. This

catastrophic failure mode was effectively eliminated through hybridization in both H1 and H2 specimens. In this context, the displacement upon failure for CFRPC composites was improved by 120% and 160% as a result of hybridization for H1 and H2 specimens, respectively. The precise effect of hybridization in terms of pseudo ductility was investigated in detail through tensile tests, as discussed in Section 3.5. It is important to note the values of the flexural moduli of the thermoplastic composites are also comparable to the storage moduli values reported in Section 3.3.

A comparison of the flexural response of Elium composites with their epoxy counterparts revealed that the thermoset composite exhibited superior flexural properties to both CFRPC and GFRPC composites. The average flexural strength of the CF/epoxy composite specimens was found to be 721 MPa, this being around 9.5% more than the CF/Elium® composites. Nevertheless, the average displacement upon failure for CF/Elium® composites was found to be 25% more than that of CF/epoxy composites. Therefore, CF/Elium® specimens exhibited a relatively less catastrophic failure mode compared to their epoxy counterparts, owing to the ductile nature of the thermoplastic matrix. Based on Figure 8A, the CF/epoxy composites exhibited a sharp drop in load upon simultaneous failure of the carbon fibers and the matrix. On the other hand, the initial drop in the load – displacement curve for CF/Elium® composites (i.e., the point labeled as 1) represents the fracture of the thermoplastic matrix, followed by the progressive failure of the carbon fibers in the load – displacement curve (i.e., the point labeled as 2).

On the other hand, the GF/epoxy composites exhibited an average flexural strength of 208 MPa, 65% more than that of GF/Elium® composites. Both thermosetting and thermoplastic composite specimens exhibited typical progressive failure mode observed in GFRPC specimens. However, the average displacement upon failure for GF/Elium® composites was recorded to be 80% more than that of the epoxy counterparts. Similar to CF/Elium® composites, the point labeled as 1 in Figure 8C represents failure in the Elium® matrix, whereas the point labeled as 2 represents the start of the progressive failure of the glass fibers. A substantial decrease in the performance of the GF/Elium® composites compared to the GF/epoxy counterparts is primarily attributed to weak interface, poor bonding of the glass fibers with Elium® resin and higher void content, as discussed in detail in Section 3.1 and Section 3.6. In term of comparison with the conventional thermosetting composites, multiple studies have reported lower flexural performance of Elium® composites. For example, Bhudolia et al.[60] found that the flexural strength of CF/Elium® was decreased from 1007 to 671 MPa, showing a around 34% decrease. Similarly, the tensile strength of the infusible thermoplastic composites was also decreased by around 17% compared to that of the epoxy composites. Another study also reported similar trends in the flexural properties of the thermoplastic composites compared to the conventional thermosetting composites.[61]

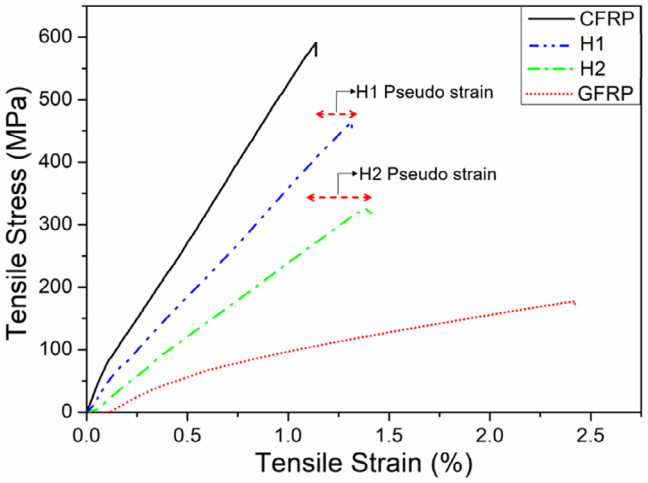

FIGURE 9 Tensile stress–strain curves for all the specimens

3.5 | Tensile tests

The tensile stress–strain curves for all the thermoplastic composite configurations are given in Figure 9, whereas Figure 10 shows typical strain contour plots achieved from DIC along with failure images. The average results for the tensile tests in terms tensile strength, failure strain and Young's modulus are provided in Table 4. It is evident from the results that the CFRPC specimens exhibited a significantly higher tensile strength (607 MPa) compared to all the other specimens. Whereas the lowest value of the tensile strength was recorded for GFRPC specimens as 180 MPa. Both H1 and H2 hybrid specimens exhibited 155% and 78% higher tensile strength, respectively, compared to the GFRPC specimens. A similar trend in the Young's modulus of the composite specimens was observed. The highest value was recorded as 59.5 GPa for CFRPC specimens, comparable to the flexural modulus (50 GPa) and the storage modulus (44.5 GPa) recorded for the CFRPC specimens in previous sections.

The strain contours show the maximum strain regions (in red color) prior complete failure of the composite laminates. It can be seen in Figure 10 that the maximum strain was concentrated on the center of the CFRPC specimens and the brittle failure also occurred in

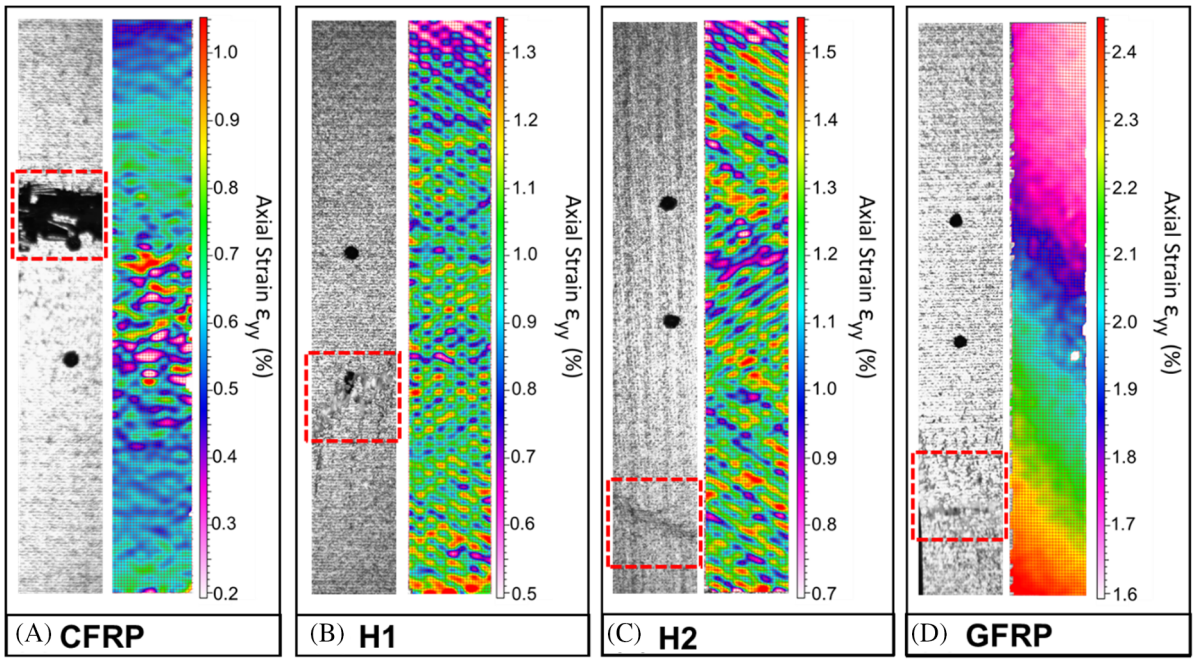

FIGURE 10 Digital image correlation results and failure modes under tensile tests

TABLE 4 Tensile properties of composite specimens

Specimen	CFRPC	H1	H2	GFRPC
Peak load (kN)	31.6 ± 0.5	18.9 ± 0.2	13.2 ± 0.3	8.6 ± 0.3
Max. tensile stress (MPa)	607 ± 7.8	459 ± 4.6	321 ± 5.3	180 ± 7.4
Max. tensile strain (%)	1.09 ± 0.04	1.28 ± 0.03	1.49 ± 0.03	2.43 ± 0.1
Young's modulus (GPa)	59.5 ± 0.2.1	35.7 ± 0.8	21.5 ± 0.6	7.4 ± 0.2

the same region. Whereas the maximum strain in both types of hybrid specimen was randomly distributed through the specimens. In contrast to CFRPC specimens, the GFRPC samples exhibited a ductile failure where the maximum strain was introduced in the lower regions of the samples in the direction of the applied load (similar to the contours observed by Naresh et al.[62] for GFRPC epoxy composites).

It is important to note that even though CFRPC specimens demonstrated the highest tensile strength, a catastrophic failure mode was observed for these specimens with an average tensile strain of only 1.09. As result of positive hybridization effect, the tensile strain for H1 specimens increased to 1.28, showing more than 17% increase compared to the CFRPC specimens. At the same time, the pseudo-strain was increased by around 37% for H2 hybrid specimens. Failure in both hybrid specimens initiated from the central carbon fiber regions, as shown by the cross-sectional optical micrographs in Figure 11. Upon carbon failure, the applied load was carried by the high strain glass fibers, introducing pseudo strain and showing a ductile failure of the glass fibers upon complete fracture of the hybrid specimens. Therefore, the abrupt failure of carbon fibers was successfully prevented by hybridization with the glass fibers. A further fractographic analysis was conducted through SEM analysis to understand the failure modes at a microscopic level, as discussed in detail in the following section. The highest value of average tensile strain was recorded for GFRPC specimens as 2.43, more than double of the tensile strain exhibited by CFRPC specimens.

Similar tensile strength values and tensile strain trends have also been reported in the literature for carbon/glass hybrid epoxy composite specimens. For example, Naresh et al.[62] reported a tensile strain of 1.09 for CFRPC specimens which was increased to 1.30 for hybrid specimens and the highest value was recorded for GFRPC specimens as 1.82 at a strain rate of 542.4 s^{-1}. As the strain-rate was reduced in the study, the tensile strain of the specimens dramatically increased. In another study, Yu et al.[34] manufactured different hybrid composite configurations based on high strength carbon fibers, high modulus carbon fibers and high strain glass fibers with similar stacking sequences as adopted in this study and investigated the effect hybridization on pseudo

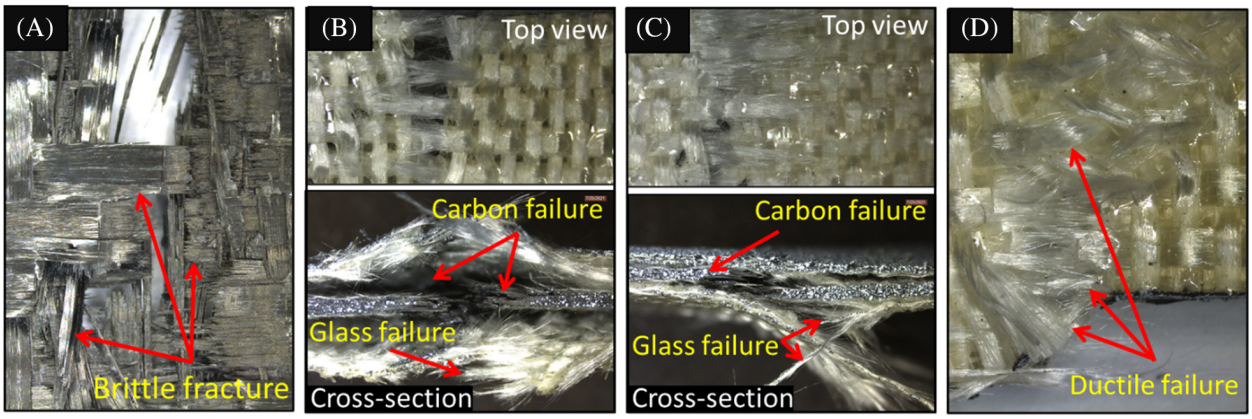

FIGURE 11 Optical micrographs of the fractured specimens after tensile tests

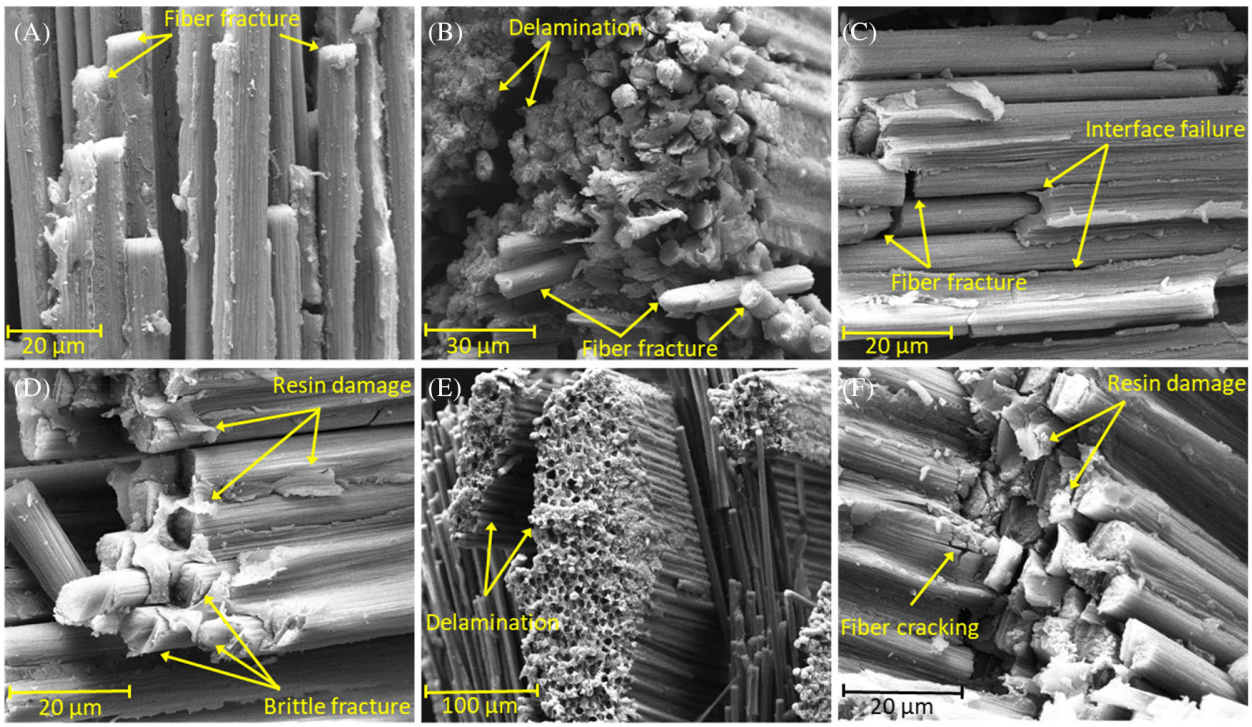

FIGURE 12 Scanning electron microscopy images after tensile tests for carbon fiber reinforced polymer composite specimens

strain in each configuration. The hybrid composite specimens based on high strength carbon and glass fibers showed similar straight stress–strain curves as shown in Figure 10, as no substantial carbon fiber fragmentation was observed before the complete failure of the hybrid laminates. Another reason for the low pseudo gain was the marginal difference between the failure strains of carbon (1.47%) and glass fibers (1.94%). One the other hand, the hybrid specimens based on high modulus carbon fibers and glass fibers exhibited a remarkable pseudo ductile behavior. In this study, the premature failure of Elium resin was observed to be one of the limiting factors to achieve high pseudo gains in the hybrid specimens.

3.6 | Scanning electron microscopy

The failure of the composite specimens subjected to mechanical testing was investigated in detail at a microscopic level using the SEM technique. The SEM images of the fractured CFRPC Elium® composites are shown in Figure 12. As evident from the XCT analysis and the mechanical performance, the CFRPC specimens exhibited a very strong CF-Elium® interface. As a result of this strong interface, the CFRPC specimens subjected to flexural and tensile tests exhibited a dominant brittle failure mode. Failure in all the CFRPC specimens comprised of fiber fracture, resin damage and cracks, delamination

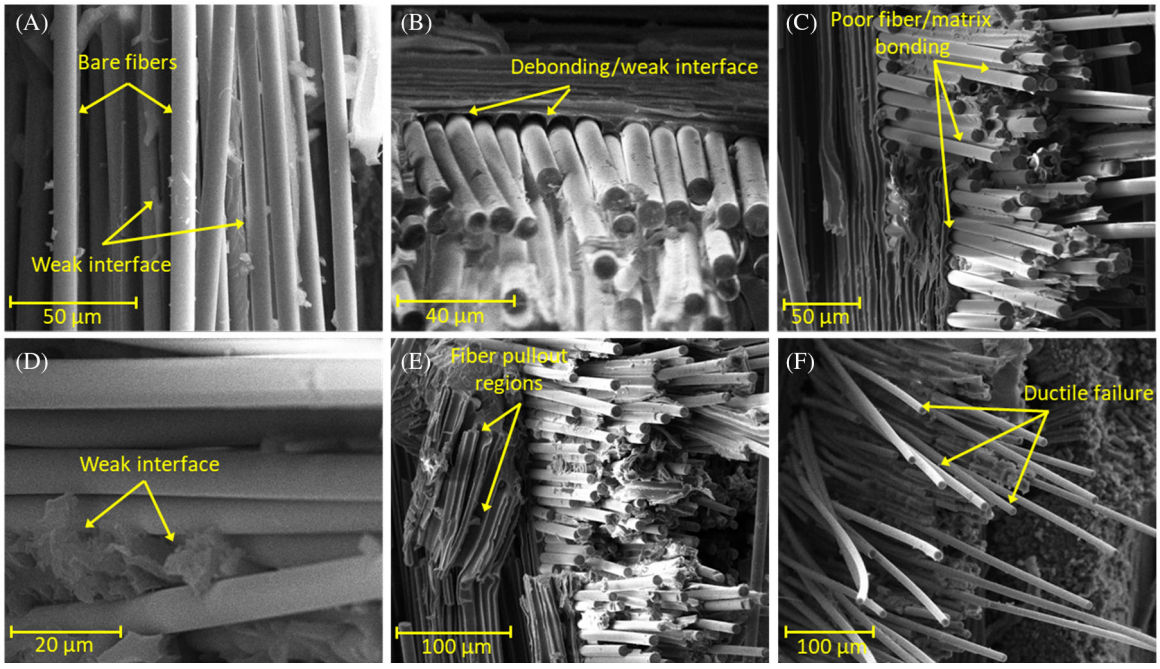

FIGURE 13 Scanning electron microscopy images after tensile tests for glass fiber reinforced polymer composite specimens

and fiber cracking. A number of studies have also reported similar failure modes in traditional CFRPC composites.[17,63] Apart from the above-mentioned failure modes, the SEM images also revealed resin damage in terms of the river line patterns. As reported previously, one of the main reason for superior bonding between CFs and the matrix is the higher roughness of the carbon fibers and their smaller diameter compared to the GFs.[17] A strong bond is developed due to mechanical interlocking as the surface roughness raises the surface area/unit volume of the fibers. The SEM images in Figure 12 show that the CFs remained intact with Elium® resin even after complete fracture and the specimens exhibited a combined brittle failure mode for CFs and the matrix.

As observed in previous sections, GFRPC specimens exhibited low mechanical properties compared to the CFRPC composites. The XCT analysis also showed that as the number of glass fiber layers was increased, the void content significantly increased. Furthermore, it has been reported in our previous study that the glass fabrics have higher weave/tow density compared to carbon fibers.[17] This high weave density can reduce the permeability of the preform and lead to poor interfacial bonding, having a negative influence on the mechanical performance of GFRPC composites. This weak fiber – matrix interface was also observed through SEM micrographs of fractured GFRPC composites (Figure 13). Upon complete fracture, individual glass fibers showed a complete ductile failure unlike brittle failure observed for carbon fibers in CFRPC specimens (Figure 13F). A number of articles in the literature have described similar failure modes in GFRPC composites.[58,62]

The SEM micrographs revealed a dominant fiber pullout failure mode throughout multiple regions of the fractured GFRPC samples. This is primarily associated with the weaker fiber – matrix interface. Due to weaker interfacial bonding, the glass fibers were easily detached from the thermoplastic matrix at a microscopic level (Figure 13B). Multiple bare fibers were also observed throughout the fractured specimens due to poor bonding between the glass fibers and Elium® resin (Figure 13A,D). As reported previously, weak bonding between the GFs and the matrix resulted in fiber pullout failure mode in GFRPC Elium® composites. Fiber pullout was further pronounced upon loading in tensile tests and different regions of the fractured specimens showed complete fiber pullout (Figure 13E). Along with this, increased void content also plays an important role in fracture of the specimens. Voids can act as crack initiation sites in the matrix. A small force can result in propagation of these cracks throughout the composite laminate, resulting in delamination and fracture. Therefore, high void content and weak interfacial bonding are two critical parameters that can decrease the overall mechanical performance in terms of tensile strength, flexural strength and modulus. A decrease in the overall void content and stronger fiber – matrix bonding can ensure superior mechanical properties. Along with this, fiber orientation in the composite specimens can also be tailored to get the desired properties.

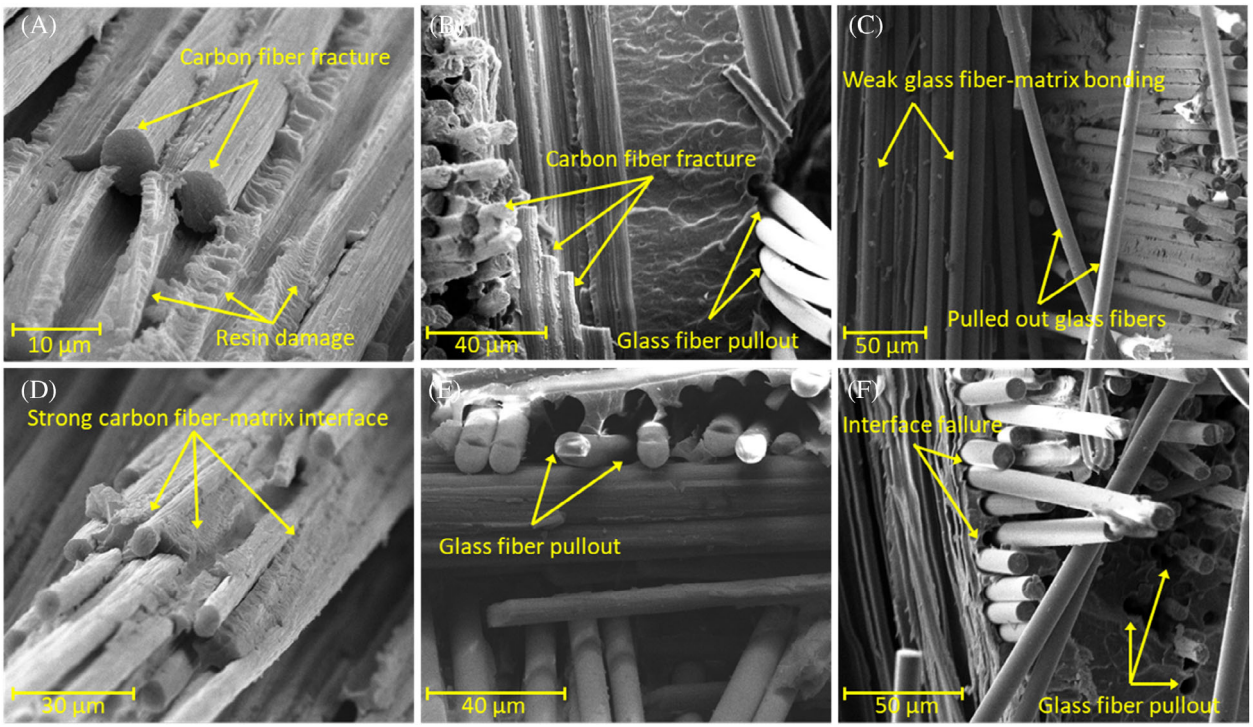

FIGURE 14 Scanning electron microscopy images after tensile tests for (A–C) H1 specimens and (D–F) H2 specimens

Both types of hybrid specimen exhibited mixed failure modes observed for pure CFRPC and GFRPC composites. The micrographs for the fractured H1 specimens subjected to tensile tests are shown in Figure 14A–C, whereas those for the H2 specimens are shown in Figure 14D–F. The carbon fibers and the glass fibers were easily identified in both types of hybrid specimen based on the difference in the fiber diameter, surface roughness and failure modes. The CFs showed strong fiber-matrix interface in the hybrid specimens (Figure 13A,D) and exhibited a brittle failure. A severe resin damage was also observed in the region having carbon fibers. In contrast, the GFs exhibited a prominent fiber pullout failure mode along with debonding and delamination (Figure 14B,E). Just like GFRPC specimens, bare GFs, weak fiber – matrix interface and interface failure were observed in multiple regions of the hybrid specimens containing glass fibers (Figure 14C,F). Along with this, delamination between two types of fabrics was also observed in both types of hybrid specimens. A number of studies in the literature have reported similar failure modes for carbon/glass hybrid composite laminates.[17,58]

It is important to note that the CFs in the hybrid samples contributed to a better interfacial bonding and the hybrid specimens exhibited a significantly stronger microstructural stability than the GFRPC specimens. Whereas the introduction of more ductile GFs in the hybrid samples eliminated the catastrophic brittle fracture affiliated with pure CFRPC composite. It has been well-established in the literature that the brittle fracture observed in CFRPC composites can be effectively avoided by hybridization with high strain GFs, without a major compromise on strength.[64]

4 | CONCLUSIONS

In this research, the effect of hybridization on the microstructure and mechanical performance of carbon/glass hybrid Elium® composites was investigated. Two types of hybrid composite specimens were manufactured along with CFRPC and GFRPC to introduce pseudo-ductility and avoid the catastrophic CFRPC failure. A detailed XCT study was conducted to visualize the microstructure and to study the effect of hybridization on the evolution of fiber volume fraction and defects such as voids and porosity. The thermal stability of specimens was investigated by the TGA analysis and the thermomechanical properties were studied by conducting the DMA tests. The mechanical performance was investigated in detail through flexural and tensile tests, and the fractographic study comprised of optical microscopy and SEM.

The XCT investigation revealed that the void content substantially increased as the number of glass fabric layers were increased, due to high weave density of the glass fabrics and weaker glass fiber-matrix interface. The highest void content was recorded as 1.24% in GFRPC specimens whereas the CFRPC specimens exhibited a microporosity content of only 0.28%. As the glass fiber content was increased in the hybrid specimens, the void

percentage was substantially increased and this had a negative influence their mechanical performance. The highest storage modulus, flexural and tensile strengths were recorded for the CFRPC specimens. The average flexural strength for one of the hybrid configurations was observed to increase by 254% compared to pure GFRPC specimens. Similarly, the tensile strength and Young's modulus of the hybrid specimens showed 155% and 380% increase, respectively, compared to the GFRPC specimens. At the same time, The tensile strain of one of the hybrid configurations was improved by 37%, completely eliminating the catastrophic CFRPC failure. However, further pseudo gain in tensile strain was constrained due to the premature failure of Elium® resin and poor glass fiber-matrix interface. The SEM images showed fiber fracture and brittle failure modes in CFRPC specimens in contrast to fiber pullout, interfacial failure, poor fiber – matrix bonding and ductile failure modes in GFRPC specimens. The results of the study revealed that hybridization in the infusible thermoplastic composites can be successfully used to avoid the catastrophic failure in CFRPC specimens as well as to enhance the mechanical properties of the GFRPC specimens. However, the bonding between the GFs and the infusible thermoplastic resin can be improved for further enhancements in the mechanical properties of the hybrid specimens.

ACKNOWLEDGMENTS

This work is funded by the internal grant CIRA-2020-007 of Khalifa University of Science and Technology. The authors would like to thank Arkema, China for providing the Elium® resin.

DATA AVAILABILITY STATEMENT

The data that support the findings of this study are available from the corresponding author upon reasonable request.

ORCID

Tayyab Khan https://orcid.org/0000-0001-5840-4356
Umer Rehan https://orcid.org/0000-0001-5005-7855

REFERENCES

[1] T. Khan, M. A. Ali, M. S. Irfan, K. A. Khan, K. Liao, R. Umer, *Polym. Compos.* **2022**, *43*(5), 2924.
[2] T. Khan, M. S. Irfan, W. J. Cantwell, R. Umer, *Compos. Part A: Appl. Sci. Manuf.* **2022**, *156*, 106896.
[3] M. S. Irfan, R. A. Alia, T. Khan, W. J. Cantwell, R. Umer, *J. Thermoplast. Compos. Mater.* **2021**. https://doi.org/10.1177/08927057211051773
[4] M. Bunea, A. Cîrciumaru, M. Buciumeanu, I. G. Bîrsan, F. S. Silva, *Compos. Sci. Technol.* **2019**, *169*, 242.
[5] T. Khan, V. Acar, M. R. Aydin, B. Hülagü, H. Akbulut, M. Ö. Seydibeyoğlu, *Polym. Compos.* **2020**, *41*(6), 2355.
[6] M. S. Irfan, T. Khan, T. Hussain, K. Liao, R. Umer, *Compos. Part A: Appl. Sci. Manuf.* **2021**, *141*, 106236.
[7] M. Giżyński, B. Romelczyk-Baishya, *J. Thermoplast. Compos. Mater.* **2019**, *34*, 089270571983945.
[8] J. H. Eun, D. H. Kim, J. S. Lee, *Compos. Part A: Appl. Sci. Manuf.* **2020**, *137*, 105987.
[9] M. Fotouhi, M. Jalalvand, M. Saeedifar, B. Xiao, M. R. Wisnom, *Compos. Struct.* **2020**, *247*, 112444.
[10] S. G. Marino, G. Czél, *Compos. Part A: Appl. Sci. Manuf.* **2021**, *142*, 106233.
[11] X. Yan, Y. Yang, H. Hamada, *Polym. Compos.* **2018**, *39*(10), 3564.
[12] C. Thiyagu, U. Narendrakumar, *Polym. Compos.* **2022**, *43*(3), 1395.
[13] G. Rajaraman, S. K. Agasti, M. P. Jenarthanan, *Polym. Compos.* **2020**, *41*(3), 994.
[14] H. Zhang, X. Gao, H. Li, W. Wu, S. Sun, *Polym. Compos.* **2021**, *42*(10), 5348.
[15] Ö. Y. Bozkurt, A. Erkliğ, M. Bulut, *Polym. Compos.* **2018**, *39*(2), 467.
[16] A. Ichenihi, W. Li, Y. Gao, *Polym. Compos.* **2021**, *42*(12), 6764.
[17] T. Khan, A. Fikri, M. S. Irfan, E. Gunister, R. Umer, *J. Compos. Mater.* **2020**, *55*(12), 1635.
[18] C. Dong, I. J. Davies, *Mater. Des.* **2012**, *37*, 450.
[19] S. Dasari, S. Saurabh, R. K. Prusty, *J. Appl. Polym. Sci.* **2021**, *138*(9), 49928.
[20] M. Derradji, J. Wang, W. Liu, *Phthalonitrile Resins and Composites*. William Andrew, Norwich, New York **2018**, p. 241. https://doi.org/10.1016/B978-0-12-812966-1.00005-6
[21] Y. Swolfs, Y. Meerten, P. Hine, I. Ward, I. Verpoest, L. Gorbatikh, *Compos. Struct.* **2015**, *131*, 259.
[22] M. Fotouhi, J. Fuller, M. Longana, M. Jalalvand, M. R. Wisnom, *Compos. Struct.* **2019**, *215*, 365.
[23] G. Czél, T. Rev, M. Jalalvand, M. Fotouhi, M. L. Longana, O. J. Nixon-Pearson, M. R. Wisnom, *Compos. Part A: Appl. Sci. Manuf.* **2018**, *104*, 151.
[24] Y. Swolfs, L. Gorbatikh, I. Verpoest, *Compos. Part A: Appl. Sci. Manuf.* **2014**, *67*, 181.
[25] M. A. Caminero, G. P. Rodríguez, J. M. Chacón, I. García-Moreno, *Polym. Compos.* **2019**, *40*(9), 3678.
[26] Y. Liu, X. Zhou, Z. Jia, H. Wu, G. Wu, *Adv. Funct. Mater.* **2022**, *32*(34), 2204499.
[27] J. Liu, Z. Jia, Y. Dong, J. Li, X. Cao, G. Wu, *Mater. Today Phys.* **2022**, *27*, 100801.
[28] Z. Jia, M. Kong, B. Yu, Y. Ma, J. Pan, G. Wu, *J. Mater. Sci. Technol.* **2022**, *127*, 153.
[29] S. Zhang, Z. Jia, B. Cheng, Z. Zhao, F. Lu, G. Wu, *Adv. Compos. Hybrid Mater.* **2022**, *5*, 2440.
[30] Z. Zhao, W. Liu, Y. Jiang, Y. Wan, R. Du, H. Li, *J. Cleaner Prod.* **2022**, *359*, 132134.
[31] M. Jalalvand, M. Fotouhi, M. R. Wisnom, *Compos. Sci. Technol.* **2017**, *153*, 232.
[32] C. Huang, M. W. Joosten, *Compos. Part A: Appl. Sci. Manuf.* **2021**, *146*, 106403.
[33] G. Czél, M. Jalalvand, M. R. Wisnom, *Compos. Struct.* **2016**, *143*, 362.
[34] H. N. Yu, M. L. Longana, M. Jalalvand, M. R. Wisnom, K. D. Potter, *Compos. Part A: Appl. Sci. Manuf.* **2018**, *105*, 40.
[35] K. Tayyab, *J. Aerosp. Eng. Mech.* **2019**, *3*(1), 156. https://doi.org/10.36959/422/435
[36] H. Parmar, T. Khan, F. Tucci, R. Umer, P. Carlone, *Mater. Manuf. Processes* **2021**, *37*(5), 483.

[37] T. Khan, A. R. Aziz, M. S. Irfan, W. J. Cantwell, R. Umer, *J. Compos. Mater.* **2022**, *56*(9), 1335.
[38] C. Gomez, D. Salvatori, B. Caglar, R. Trigueira, G. Orange, V. Michaud, *Compos. Part A: Appl. Sci. Manuf.* **2021**, *147*, 106448.
[39] W. Obande, D. Mamalis, D. Ray, L. Yang, C. M. Ó. Brádaigh, *Mater. Des.* **2019**, *175*, 107828.
[40] H. Yaghoobi, F. Taheri, *Polym. Compos.* **2021**, *42*(9), 4660.
[41] G. Fredi, A. Dorigato, A. Pegoretti, *Polym. Compos.* **2019**, *40*(9), 3711.
[42] D. S. Cousins, Y. Suzuki, R. E. Murray, J. R. Samaniuk, A. P. Stebner, *J. Cleaner Prod.* **2019**, *209*, 1252.
[43] R. E. Murray, J. Roadman, R. Beach, *Renewable Energy* **2019**, *140*, 501.
[44] M. E. Kazemi, L. Shanmugam, D. Lu, X. Wang, B. Wang, J. Yang, *Compos. Part A: Appl. Sci. Manuf.* **2019**, *125*(June), 105523.
[45] B. Miranda Campos, S. Bourbigot, G. Fontaine, F. Bonnet, *Polym. Compos.* **2022**, *43*(5), 2485.
[46] M. A. Ali, R. Umer, K. A. Khan, *Int. J. Lightweight Mater. Manuf.* **2020**, *3*(3), 204.
[47] M. A. Ali, R. Umer, K. A. Khan, S. Bickerton, W. J. Cantwell, *Aerosp. Sci. Technol.* **2018**, *82–83*, 520.
[48] M. A. Ali, R. Umer, K. A. Khan, *CT Scan Generated Material Twins for Composites Manufacturing in Industry 4.0* Springer Nature, Singapore **2020**, p. 73. https://doi.org/10.1007/978-981-15-8021-5_4
[49] M. A. Ali, R. Umer, K. A. Khan, W. J. Cantwell, *Compos. Sci. Technol.* **2019**, *184*, 107828.
[50] T. Khan, O. A. Aydın, V. Acar, M. R. Aydın, B. Hülagü, H. Bayrakçeken, M. Ö. Seydibeyoğlu, H. Akbulut, *Mater. Today Commun.* **2020**, *24*, 101233.
[51] K. Naresh, K. Shankar, R. Velmurugan, *Int. J. Polym. Anal. Charact.* **2018**, *23*(8), 684.
[52] S. Gurusideswar, R. Velmurugan, N. K. Gupta, *Int. J. Impact Eng.* **2017**, *110*, 324.
[53] H. Lu, P. D. Cary, *Exp. Mech.* **2000**, *40*(4), 393.
[54] A. Hendlmeier, L. I. Marinovic, S. Al-Assafi, F. Stojcevski, L. C. Henderson, *Compos. Part A: Appl. Sci. Manuf.* **2019**, *127*, 105622.
[55] Sizing for carbon fiber | CompositesWorld. https://www.compositesworld.com/articles/sizing-for-carbon-fiber (accessed Sep. 11, 2022).
[56] R. Umer, M. A. Ali, R. A. Alia, K. A. Khan, W. J. Cantwell, *Mater. Today Commun.* **2020**, *25*, 101419.
[57] M. A. Ali, R. Umer, K. A. Khan, W. J. Cantwell, *Compos. Sci. Technol.* **2019**, *173*, 99.
[58] D. K. Rathore, R. K. Prusty, S. C. Mohanty, B. P. Singh, B. C. Ray, *Mech. Mater.* **2017**, *105*, 99.
[59] Standard test methods for flexural properties of unreinforced and reinforced plastics and electrical insulating materials. https://www.astm.org/d0790-17.html (accessed Aug. 17, 2022).
[60] S. K. Bhudolia, P. Perrotey, S. C. Joshi, *J. Sports Eng. Technol.* **2015**, *230*(2), 64.
[61] S. K. Bhudolia, S. C. Joshi, A. Bert, B. Yi Di, R. Makam, G. Gohel, *Compos. Commun.* **2019**, *13*, 129.
[62] K. Naresh, K. Shankar, B. S. Rao, R. Velmurugan, *Compos. B Eng.* **2016**, *100*, 125.
[63] P. Vimalanathan, N. Venkateshwaran, S. P. Srinivasan, V. Santhanam, M. Rajesh, *Int. J. Polym. Anal. Charact.* **2018**, *23*(2), 99.
[64] J. Zhang, K. Chaisombat, S. He, C. H. Wang, *Mater. Des. (1980-2015)* **2012**, *36*, 75.

How to cite this article: T. Khan, M. A. Ali, M. S. Irfan, W. J. Cantwell, U. Rehan, *Polym. Compos.* **2023**, *44*(3), 1859. https://doi.org/10.1002/pc.27210